5 Solar cycle evolution of small photospheric magnetic elements

5.1 Introduction

In Chapter 4 we determined the contrast of small photospheric bright features, active region faculae and the network, as a function of both heliocentric angle and magnetogram signal, and we obtained an analytical function that predicts their contrast. The study was performed using data from ten days during 1999, therefore, it did not consider any temporal evolution with the solar cycle. Now we consider one more variable − time − and we will analyze the solar cycle evolution of these magnetic elements through the rising phase of solar cycle 23.

As has been mentioned throughout, the solar irradiance changes on a variety of time-scales, mainly arising from the changing presence and evolution of magnetic features over the solar disk. Active regions are considered to be the main drivers of total and spectral irradiance variations on time-scales of a solar rotation. However, this breaks down for variations on solar cycle time-scales because on this time-scale it exists a variation of about 0.1% from minimum to maximum. Different mechanisms have been proposed to explain these variations, among them, the small-scale magnetic elements that compose the enhanced and the quiet network. It is mostly expected that such small elements contribute substantially to the increase of the observed irradiance during activity maximum (Foukal et al. 1991; Foukal & Lean 1988; Lean et al. 1998; Fligge et al. 2000a; Solanki & Fligge 2002), while other authors have worked out different mechanisms (Kuhn et al. 1988; Balmforth et al. 1996). Thus, nowadays the origin of these long-term variations between activity minimum and maximum is still under debate.

Solar irradiance variations reflect the existence of several distinct physical processes continously at work in the solar interior. The interpretation of these processes contribute to a better knowledge of stellar structure, particularly, the irradiance variations may help us to understand solar rotation, convection and magnetism. Nevertheless, they are not fully understood, being one of the most controversial and unknown aspects in these long-term variations the contribution of the small scale features. It is our aim in this Chapter to contribute to a better knowledge of the solar variability associated with the eleven year cycle.

Figure 5.1 displays the total solar irradiance variations from 1996 to 2001, i.e., through the rising phase of the present solar cycle. Most of the plotted data come from the DIARAD and PMO6-V radiometers on board SOHO; ACRIM II data (Willson 1994) are used to fill the gap during the SOHO vacations in 1998 and early 1999. Thanks to its large, stable and homogeneous data sets, SOHO provides us a unique opportunity to study the first half of the present magnetic cycle. In particular, we have analyzed the evolution of the intensity contrast of small magnetic features − from faculae to the magnetic network − as a function of position, magnetic signal and time, in order to study their relative contribution to the solar cycle irradiance variations. Thus, we implicitly infer that the physical properties of the flux tubes underlying these magnetic features are time-independent. To our knowledge, no similar work has been done before. We have also found that the time evolution of the magnetic field distribution follows a power-law behaviour that changes every year; this result has allowed us to quantify the populations of bright features along the solar cycle. Finally, we have proceeded to separate magnetic field maps into two components, active regions and quiet Sun areas, and we have examined the contrast evolution of both components. Using this magnetogram decomposition, we have quantified the evolution of the network and the facular populations, and then, we have been able to compare their role in the long-term irradiance variations. We will show that the network is always present over the solar disk, becoming the dominant component through the solar cycle, including the activity maximum period, and in spite of having a lower increase rate relative to that of faculae. To carry out these investigations it has been necessary to perform a careful analysis of the detector's response along the rising phase of cycle 23.

In Section 5.2 we present the data sets used and the analysis procedures. In Section 5.3 we describe the results. They are discussed in Section 5.4, which also presents the conclusions of this study.
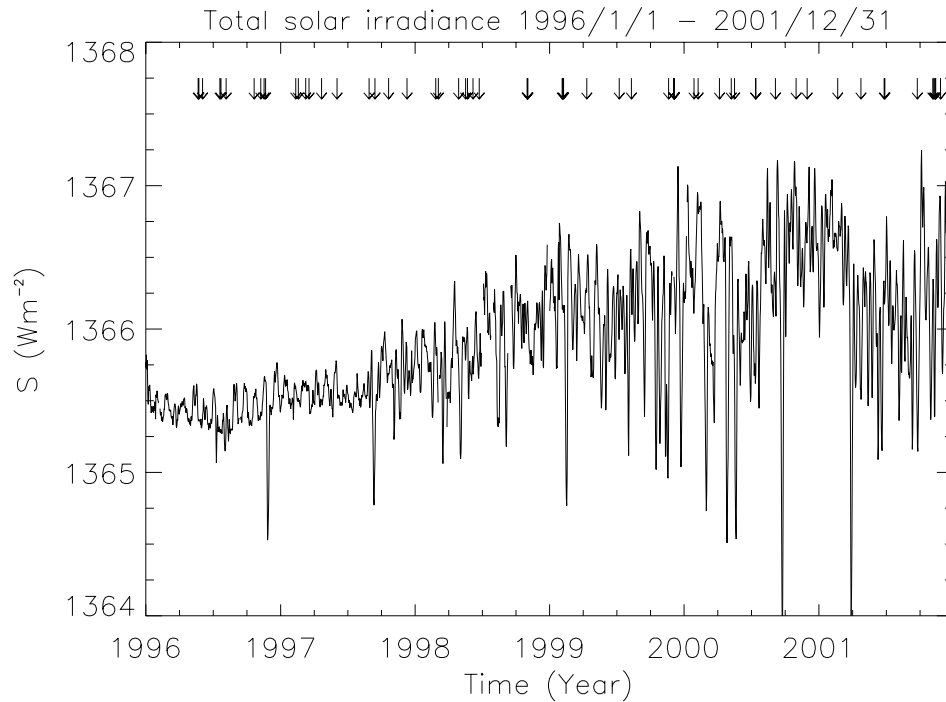
Figure 5.1: Total solar irradiance variations between 1996 and 2001. This period covers beyond the rising phase of solar cycle 23; note the double peak at the end of the plotted period. Arrows mark the sixty days selected for this study, distributed along the six years period. This figure was done using version d25_06_030 of the irradiance composite described in Fröhlich & Lean (1998a) and unpublished data from VIRGO/SOHO (the PMOD/WRC, Switzerland, is acknowledged).

5.2   Data and analysis procedure

5.2.1   Data sets

The analyzed data are nearly simultaneous full disk magnetograms and continuum intensity images, recorded on sixty days (ten images per year) spread during the rising phase of solar cycle 23, spanning from the 1996 minimum to 2001, one year after the solar maximum. These days were chosen because they contain everything from almost field-free quiet Sun periods to intense active regions; the sample contains magnetic activity spread over almost all $\mu = \cos\theta$ values. Selected days have been marked by arrows in figure 5.1, and table 5.1 shows their main characteristics. The date and time of the observations for the magnetograms and their corresponding averaged intensities (see Section 5.2.2) are given there. The time for the intensities

corresponds to the middle of the 5-minute integration time. We also indicate the time difference between each magnetogram and its intensity pair, as well as the integration time for every magnetogram and the angle of the solar North Pole on the images (we will clarify these last points in Section 5.2.3).

We also employed twelve series of the high rate one-hour data sets (sixty magnetograms each with a cadence of one minute) in order to study the temporal variation of the noise level in Section 5.2.2.

5.2.2   Reduction method and analysis

We have employed averages over five single consecutive intensity images, taken at a cadence of one per minute, in order to avoid $p-$mode oscillations in the intensity. Individual intensity images were firstly corrected for limb-darkening effects, as described in Section 4.2.2; then, each of them was rotated to co-align with the corresponding magnetogram, before the averaging. Care has been taken to use intensity images obtained as close in time to the magnetograms as possible. In all cases but six, the two types of images were recorded within 30 minutes of each other, only in one case the time difference was higher (74 minutes); the reason was that there were not available intensities closer in time to their corresponding magnetogram. Twenty-three out of the sixty image pairs were exactly simultaneous. Magnetograms are either 1 or 5-minute averages, taken at a cadence of 96 minutes (see Section 5.2.3). Our final data sets are pairs of co-aligned averaged magnetograms and averaged photospheric continuum intensity images for each of the sixty selected days that can be compared pixel by pixel.

We have determined the 1-σ noise level of the MDI magnetograms and continuum images as a function of position over the CCD array following the procedure described in Chapter 4. A fundamental aspect of this analysis is to carry out a careful study of the temporal dependence of the MDI sensitivity and stability, in order to detect the small variations in the facular and network contrasts along the rising phase of cycle 23. This is a key point, as we intend to detect magnetic signals and intensities which are only slightly higher than the signal-to-noise ratio. Any variation in the response of the detector would jeopardize our measurements. Therefore, we have determined the noise levels for each of the six years independently, in order to check the instrumental time dependence.

Table 5.1: Characteristics of the selected images from 1996 to 2001. The MDI day (first column), date (second column) and UT time is given for the magnetograms (t_{mag}, third column) and their corresponding averaged intensities (t_{int}, fourth column). Next columns show the time difference between each magnetogram and its averaged intensity pair (fifth column), the integration time of the magnetogram (sixth column) and the spacecraft roll (seventh column).

MDI day	Date	t_{mag} (UT)	t_{int} (UT)	$t_{mag} - t_{int}$ (min.)	Integration time	Angle
1996						
1237	22/05	00:00	00:32	-32	1-min	0
1239	24/05	00:04	01:18	-74	5-min	0
1249	03/06	12:48	12:44	4	1-min	0
1296	20/07	22:28	22:28	0	5-min	0
1299	23/07	01:40	01:40	0	5-min	0
1313	06/08	16:00	16:02	-2	1-min	0
1389	21/10	19:11	19:12	-1	1-min	0
1407	08/11	19:12	18:56	16	1-min	0
1416	17/11	11:15	11:14	1	5-min	0
1420	21/11	01:39	01:27	12	5-min	0
1997						
1502	11/02	06:27	06:26	1	5-min	0
1509	18/02	14:27	14:26	1	5-min	0
1529	10/03	17:36	17:19	17	1-min	0
1538	19/03	00:00	00:08	-8	1-min	0
1572	22/04	11:16	11:16	0	5-min	0
1614	03/06	11:16	11:16	0	5-min	0
1701	29/08	03:15	03:14	1	5-min	0
1717	14/09	16:00	16:02	-2	1-min	0
1754	21/10	06:23	06:20	3	1-min	0
1804	10/12	14:23	14:23	0	1-min	0
1998						
1882	26/02	18:37	18:34	3	1-min	0
1889	05/03	01:39	02:02	-23	5-min	0
1944	29/04	12:47	12:47	0	1-min	0
1963	18/05	11:11	11:11	0	1-min	0
1968	23/05	06:23	06:23	0	1-min	0
1983	07/06	03:15	02:30	45	5-min	0
2000	24/06	11:11	11:11	0	1-min	0
2130	01/11	11:11	11:11	0	1-min	9.70
2131	02/11	06:23	06:23	0	1-min	9.76
2132	03/11	06:23	06:23	0	1-min	9.84

Table 5.1: Continued.

MDI day	Date	t_{mag} (UT)	t_{int} (UT)	$t_{mag} - t_{int}$ (min.)	Integration time	Angle
1999						
2225	04/02	03:11	03:11	0	1-min	-59.23
2227	06/02	04:47	04:47	0	1-min	-59.46
2229	08/02	14:23	14:23	0	1-min	-59.74
2292	12/04	11:12	10:31	43	1-min	0
2380	09/07	17:35	17:32	3	1-min	0
2413	11/08	09:35	09:35	0	1-min	0
2514	20/11	04:48	04:22	26	1-min	0
2528	04/12	11:11	11:11	0	1-min	-69.12
2529	05/12	11:11	11:11	0	1-min	-69.11
2530	06/12	09:35	09:35	0	1-min	-69.11
2000						
2583	28/01	17:35	17:27	8	1-min	0
2594	08/02	21:32	21:33	-1	1-min	0
2652	06/04	17:35	17:12	23	1-min	0
2684	08/05	20:47	20:47	0	1-min	0
2693	17/05	20:48	21:01	-13	1-min	0
2750	13/07	22:24	22:41	-17	1-min	0
2751	14/07	00:00	00:01	-1	1-min	0
2804	05/09	19:11	19:11	0	1-min	0
2860	31/10	17:35	17:43	-8	1-min	0
2890	30/11	21:47	21:44	3	1-min	0
2001						
2973	21/02	19:11	18:56	15	1-min	0
3036	25/04	19:12	18:44	28	1-min	0
3099	27/06	16:00	16:06	-6	1-min	0
3101	29/06	20:56	20:20	36	1-min	0
3189	25/09	17:39	18:01	-22	5-min	0
3231	06/11	17:35	17:35	0	1-min	0
3234	09/11	20:47	20:53	-6	1-min	0
3237	12/11	22:26	22:33	-7	1-min	0
3239	14/11	04:51	05:30	-39	5-min	0
3252	27/11	20:47	20:47	0	1-min	0

We have applied a slightly different method to determine the noise level of the MDI images than in previous chapters, because the present data sets cover half a solar cycle. We must calculate the temporal dependence of the noise − if any − produced by the instrument itself, avoiding as much as possible potential biases due to the increasing solar activity; it is then imperative to remove any signature of solar activity. In Chapter 4 this was done by applying the removal process to several 1996 low activity magnetograms, but that method assumes that the resulting MDI noise level was time independent and remained unchanged between 1996 and 1999. Now, we are not making any a priori assumption; we will derive the noise level of the magnetogram images for each year from 1996 to 2001, and we will study its evolution.

To avoid the effects of the increasing solar activity as much as possible, we have compared two subsequent averages derived from twelve series of one-hour data sets of magnetograms spread over the six years. We took ten consecutive 1-minute magnetograms from each one-hour data set and rotated them to the center of the time series to compensate for differential rotation. Then, we have averaged separately two groups of five images each, grouping them into odds and evens. Magnetic activity over 40 G was removed in each of the two averaged magnetograms. Next step was substracting one 5-minute average from the other, in order to remove as much as possible magnetic activity. Due to the small temporal differences between the consecutive magnetograms − minimized by the fact of interchanging them −, solar activity present in both averages should be approximately the same except for minimum changes in the magnetic configuration. After this substraction the remaining fluctuations should therefore be mainly instrumental fluctuations, i.e., noise. Finally, we applied the 100×100 pixels running box described in Sections 2.4 and 4.2.2 to derive the standard deviation of the MDI magnetograms as a function of position over the CCD array. In this case, we have not masked out the limbs using an outer ring of 75 pixels width; instead, we used increasingly smaller running boxes as the limbs were approached.

The resulting standard deviation surfaces, $\sigma_{\mathrm{mag}}(x, y)$, present an increase towards the SW limb, as discussed in Chapter 4 (see figure 4.2). Hagenaar (2001) attributes this increase to wavelength gradients in the Michelson filters. This process has been carried out twice every year from 1996 to 2001, to evaluate the temporal change in the instrumental standard deviation. Figure 5.2 presents the temporal evolution of the noise level between 1996 and 2001 for the 5-minute averaged magnetograms. The
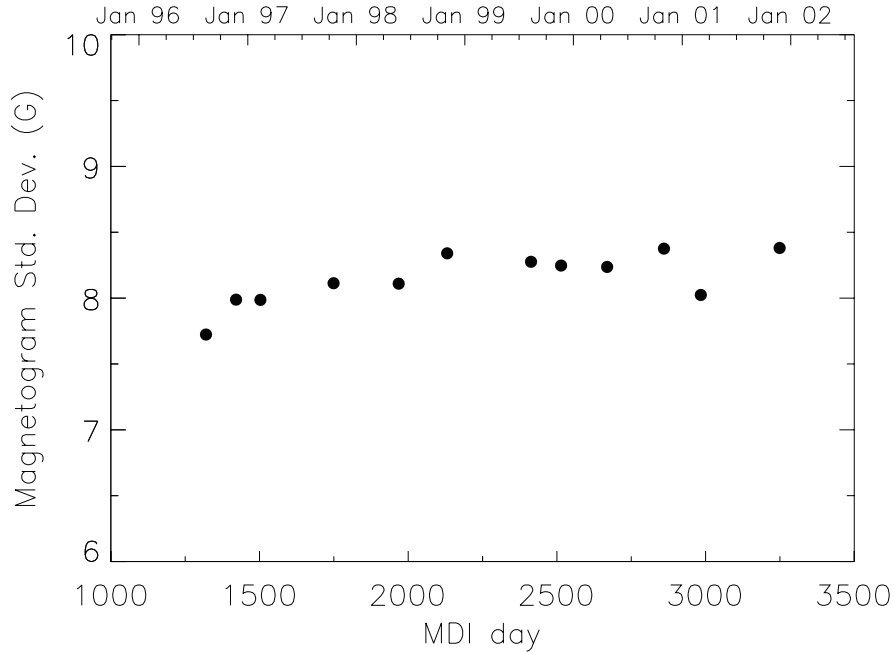
Figure 5.2: Mean of the standard deviation surfaces (in Gauss) as a function of time, calculated twice every year between 1996 and 2001. Scatter is small and hardly any trend is visible.

rounded down average value is 8 G, with a variation of 8% over the six years; only a really slightly trend is visible in this time serie, which means that the sensitivity of the detector remains almost constant all the time. To keep our calculations as accurate as possible, we have chosen the median of the two annual standard deviations corresponding to a given year, as the noise level for that year, σ^i_{mag} (where i stands for any of the six years). Note that the temporal variation of the instrumental noise could be even smaller because the calculated standard deviations may still contain some noise of solar origin, apart from the purely instrumental noise, due to magnetic fields that could have changed significantly within a few minutes.

We have also analyzed the time evolution corresponding to the mean and standard deviation of the quiet Sun intensity, $\langle I_{\mathrm{qs}} \rangle$ and σ_{Iqs} respectively, as we did in Chapter 4. The subscript qs denotes "quiet Sun". Once more, pixels with an absolute magnetic signal value below 0.5 times σ^i_{mag} have been considered as quiet Sun pixels. We have evaluated the stability of the mean non-active Sun intensity with time for the sixty selected days following a procedure similar to that applied to magnetograms. Figure 5.3 shows the normalized $\langle I_{\mathrm{qs}} \rangle$ values found; the intensity fluctuates around 2% thus, also stable enough.
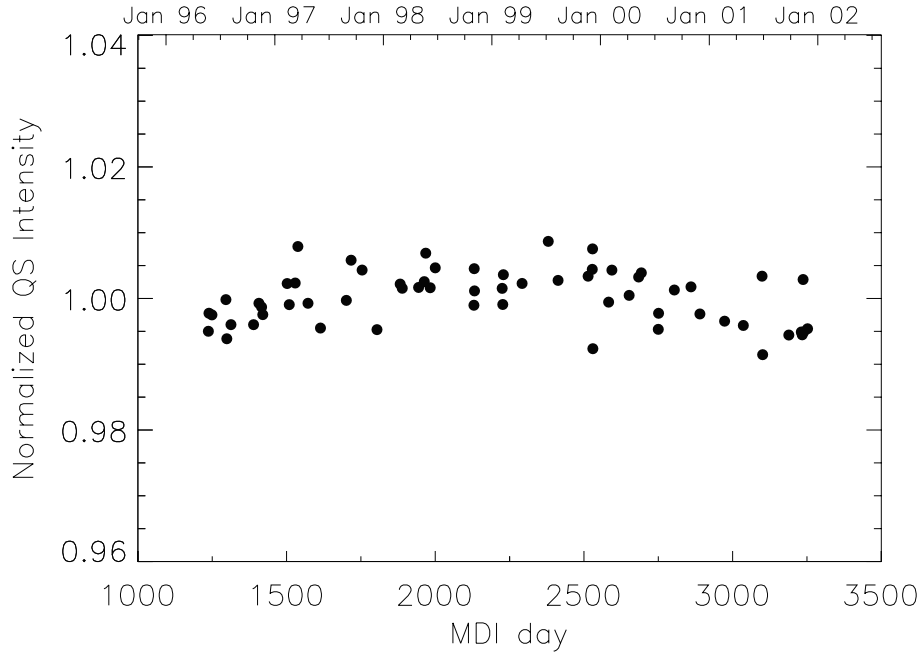
Figure 5.3: Mean normalized quiet Sun intensity for each of the sixty days considered. Fluctuations throughout the rising phase of cycle 23 are around 2%.

As in Chapter 4, the surface distribution of solar magnetic features with a bright contribution to irradiance variations is identified by setting two thresholds to every magnetogram-intensity image pair. The first threshold looks for magnetic activity of any kind, and it has been set to $\pm 3\sigma_{\mathrm{mag}}^{i}$. The second threshold masks out sunspots and pores by setting all pixels with a continuum intensity $3\sigma_{\mathrm{Iqs}}$ below the average to a null value. Note that now $\langle I_{\mathrm{qs}}\rangle$ and σ_{Iqs} are calculated on a daily basis, instead of keeping them fixed for all the period of interest as in Chapter 4. Isolated pixels have been also removed from the set. The procedure to construct a mask of the contrast of bright features for each selected day has been already described in Sections 2.4 and 4.2.2. These masks indicate the surface distribution of magnetic activity present over the solar disk at a given moment and its associated contrast, C_{fac}. As a result, we obtain the contrast, the magnetic field strength averaged over the pixel and the position for each pixel selected by these masks.

5.2.3   Technical obstacles and solutions adopted

During the analysis of the data sets described in Section 5.2.1, we have had to overcome several problems which we briefly outline here, as well as the solutions we have adopted.

The *fd_M_96m_01d* data set (freely distributed by the MDI instrument web page) was originally supposed to be composed of 5-minute averaged magnetograms, taken at a cadence of 96 minutes and giving a total of fifteen images per day; our sixty magnetograms belong to this data set. While studying their noise level we realized that, surprisingly, 1 and 5-minute magnetograms are mixed-up within the 15 daily images contained in that data set. This is denoted by the OBS_MODE keyword present in each file's header. This keyword is equal to *FD_Magnetogram* in the former case, and *FD_Magnetogram_Sum* in the later case; other keywords are also indicative of this fact. Many studies performed with this type of data only look for regions of magnetic activity, becoming then irrelevant the distinction between both kinds of magnetograms. Nevertheless, since we intend to detect low magnetic signals − just above the noise level − in order to detect network features, it is crucial to get an exact knowledge of each noise level. The integration time for each of the selected magnetograms is shown in the sixth column of table 5.1. To overcome this obstacle, we checked every header and assigned the noise level found (8 G) whenever the magnetogram had an integration time of 5 minutes, and 1.77 times that noise (rounded down, 14 G) whenever the magnetogram represented an 1-minute measurement. According to Liu & Norton (2001), the noise level of MDI magnetic measurements is 16 G for 1-minute magnetograms and 9 G for 5-minute magnetograms, from which the 1.77 factor was taken to convert between 1 and 5-minute averages. This value does not agree with the expected value of 2.23 or $\sqrt{5}$, most probably implying that points below the noise level are not only instrumental noise, but some residuals of solar origin. Before flight the noise level of single 1-minute MDI magnetograms had been estimated to be 20 G (Scherrer et al. 1995, see also table 2.3). After launch, this value was reduced to 14 G (Hagenaar 2001). We have also derived this later estimate when performing the standard deviation surface procedure to single 1-minute magnetograms, and so does Hagenaar (2001) by other means, in spite of the 16 G value reported by Liu & Norton (2001). Therefore, we will rely on the above-mentioned 14 G value.

Another obstacle we have found was a combination of sporadic changes in the orientation of the spacecraft and high temporal differences between a given magnetogram and its intensity pair. After some caveats, we identified that in nine cases (shown in column seven of table 5.1) the angular location of the solar North Pole on the CCD image did not match with the real solar North Pole, resulting in tilted images and meaning that the spacecraft was rolled with respect to its normal orientation. The angle of the solar North Pole measured eastward is given in

degrees by the SOLAR_P and P_ANGLE keywords in each file's header. In those cases, the rotation of the continuum intensity images (in order to co-align them with their corresponding magnetogram) was done in the usual westward direction, while, apparently, the solar disk was rotating with the orientation indicated by those keywords. This is specially critical when there is a high temporal difference between the two kinds of images, yielding to an impossible pixel-to-pixel comparison. The adopted solution was correcting those tilted image pairs, as well as to reselect all magnetograms that were more than 30 minutes apart from its intensity pair. For the nine tilted images, we forced that the new magnetograms were simultaneous to their respective intensities. The result of this reselection is presented in table 5.1. As already mentioned, twenty-three out of the sixty image pairs were registered simultaneously, the other pairs standing only a few minutes apart. The price paid for near-simultaneousness was the mixture of 1 and 5-minute magnetograms within the fifteen measurements recorded daily, since we outweighed simultaneousness − active features must overlap in both magnetogram and intensity images − rather than an homogeneous integration time.

5.3   Results

We have divided this Section in three parts. The first part deals with the solar cycle evolution of the contrast as a function of position over the disk and magnetic signal. The second part studies the evolution of the magnetic spectrum and fits a power-law dependence. In the third part we decompose magnetic field maps in two components and characterize the evolution of each component.

5.3.1   Solar cycle evolution of the facular contrast

Here we analyze the evolution along half a solar cycle of the AR faculae and network contrast dependence on both μ and the measured magnetic signal, B. The analysis is similar to that performed in Chapter 4, except that now it is extended in time. Remind that, we have worked with B/μ (i.e. $\langle |\mathbf{B}| \cos \gamma \rangle / \cos \theta$) instead of B, to compensate for the fact that magnetograms are only sensitive to the line-of-sight component of the magnetic field and that the magnetic field is mainly vertical. We have binned the B/μ values into eight intervals that range from the threshold level,

set at $3\sigma^i_{\mathrm{mag}}$, to 600 G; this threshold is, on average, 24 G (or 42 G for 1-minute measurements). The first four intervals are slightly different than their equivalent in Chapter 4 in order to account for the new threshold levels (see Sections 5.2.2 and 5.2.3). We distinguish between the CLV of magnetic features with different filling factor α by sorting the magnetic field strength into different bins.

Figure 5.4 represents the contrast, C_{fac}, as a function of μ for every B/μ interval during a period of solar minimum (1996). For each B/μ interval, but the last, a second degree polynomial least-squares has been fitted to guide the eye. The number in the upper left corner of each plot indicates the amount of pixels in that B/μ-bin. Figure 5.5 represents the same kind of dependence for a period of solar maximum (2001) and the complete $C_{\mathrm{fac}}(\mu)$ series − from 1996 to 2001 − is shown in Appendix C. To avoid overcrowding, we have binned the data before plotting; as the number of detected pixels grows up toward the solar maximum, the binning increases from sets of 20 points in 1996 to 40 points in 2001.

These figures, especially figure 5.5, reveal a clear evolution of the behaviour of the contrast from one B/μ interval to another. As in Chapter 4, the network features (top left panel) show a lower contrast, almost independent of μ. Oppositely, active region faculae (bottom panels) present a very pronounced CLV. Features with an intermediate magnetic signal show a gradual increase of the contrast towards the limb. Note the shift in the peak of the contrast towards lower values of μ for increasing values of B/μ; we refer to Section 4.3 for a complete discussion. Small B/μ values (< 200 G) always report a positive contrast everywhere, while it becomes negative around disk center for $B/\mu \geq 200$ G.

The corresponding plots of the contrast as a function of B/μ, for different positions on the solar disk, for each of the six years can be found in Appendix C. The solar disk has been divided into eight bins of μ that range from disk center (top panels) to the limbs (bottom panels). As commented in Chapter 4, μ-bins lying closer to the limb are wider than the ones around disk center and therefore overlap. Each point of these figures represent a binning of 40 points of data; a second degree polynomial have also been plotted, as well as a dashed line at $C_{\mathrm{fac}} = 0$. In general, the contrast initially increases with B/μ before decreasing again. The behaviour of this serie of $C_{\mathrm{fac}}(B/\mu)$ plots is similar to that presented in figure 4.4, except for some quantitative differences that will be discussed in detail in Section 5.3.1.1.

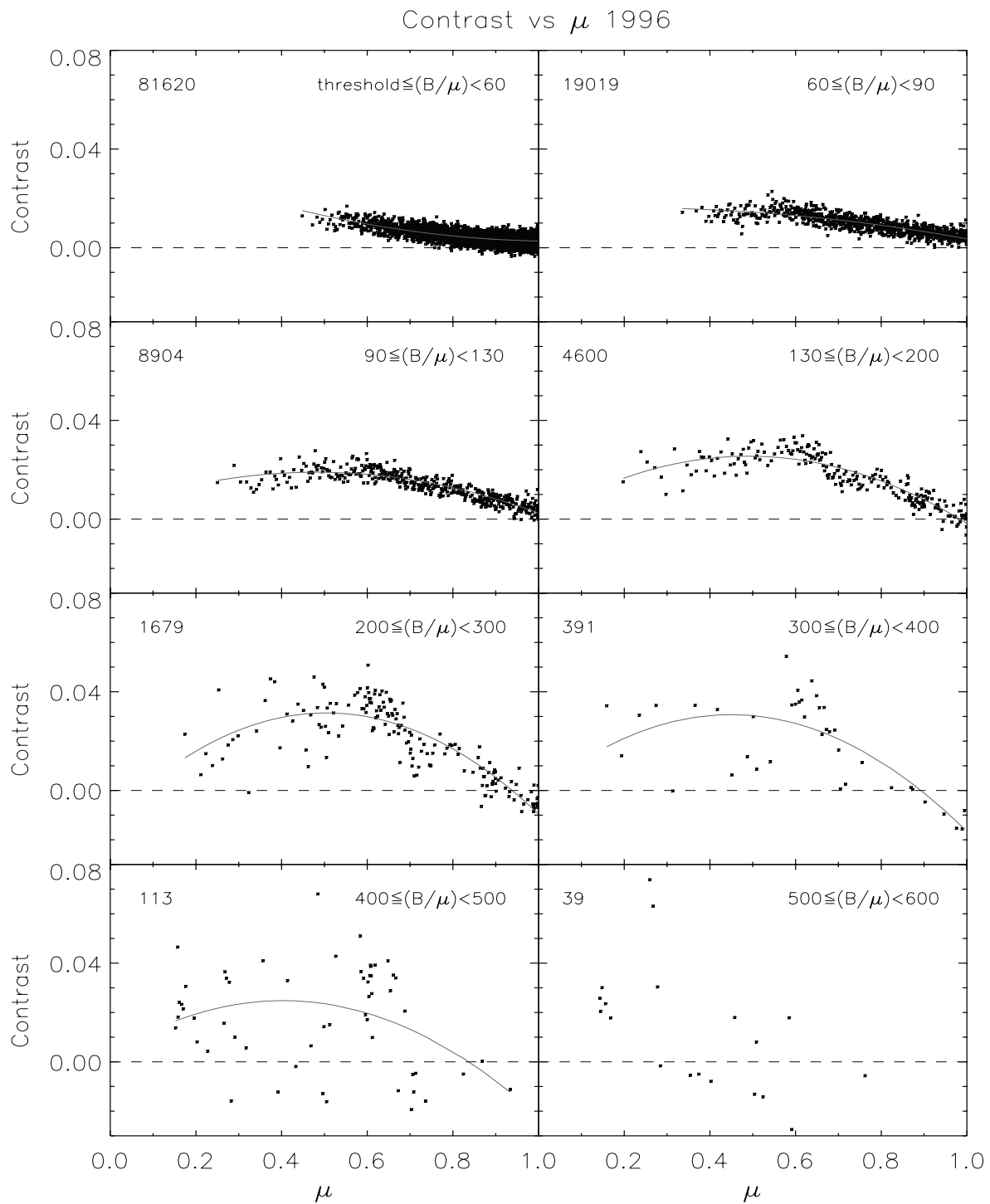By examining the temporal series of C_{fac} as a function of μ, or equivalently as

Figure 5.4: Facular and network contrast at solar minimum (1996) as a function of μ for eight magnetic field intervals, from network values (top left panel) to strong faculae (lower right). A dashed line indicates $C_{\mathrm{fac}} = 0$. Solid curves represent a second degree polynomial least-squares fit to the points; $\mu = 1$ is the disk center, $\mu = 0$ is the limb. The number in the upper left corner counts the number of pixels in each B/μ interval.
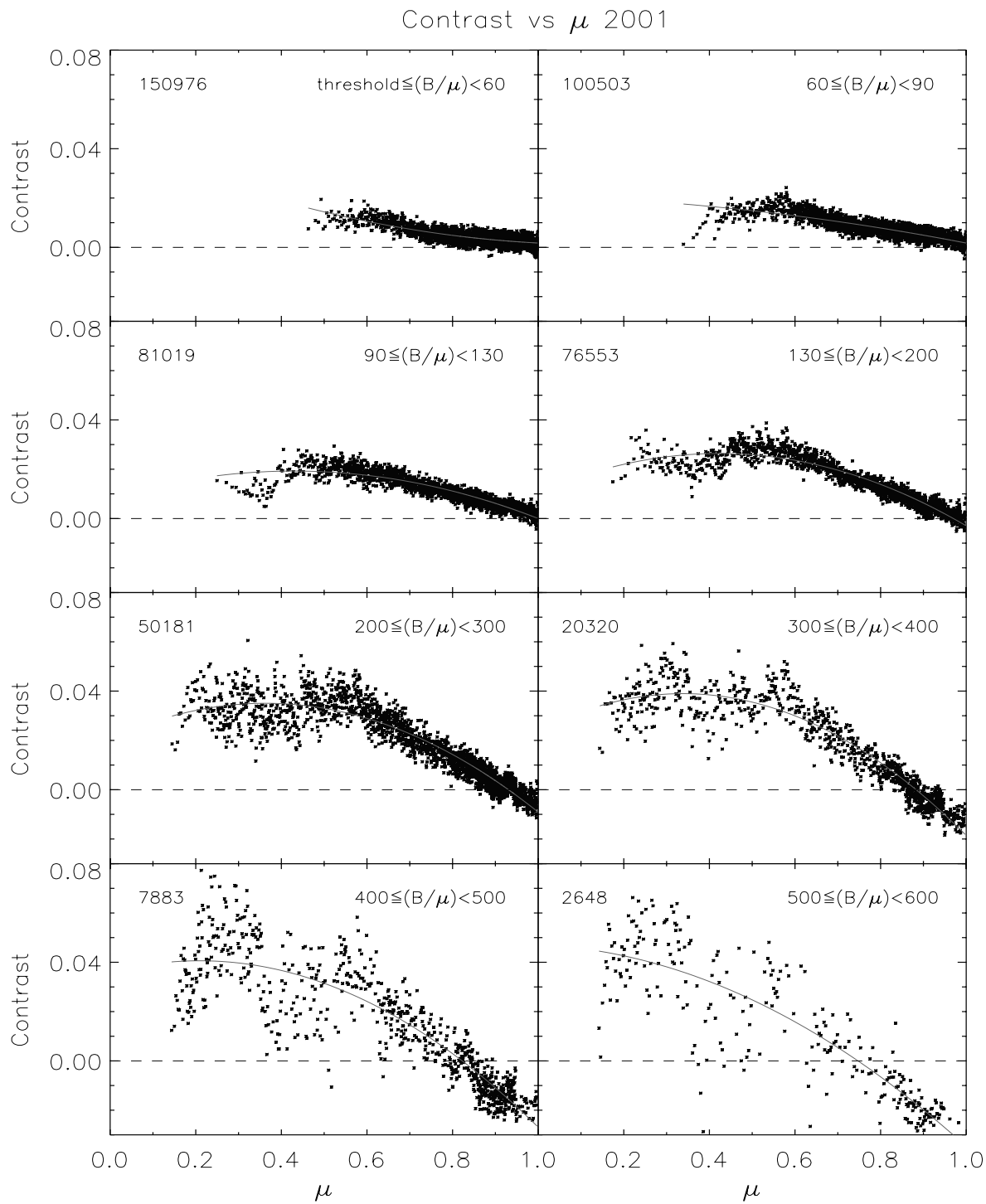
Figure 5.5: Same as figure 5.4 for a solar maximum period (2001).

a function of B/μ, it is easy to note the increase of solar activity along the rising phase of the cycle (just looking at the number of pixels). While the highest B/μ bins at solar minimum contain few points, plots are overcrowded at solar maximum. For example, low magnetic signals ($B/\mu < 90$ G, most probably belonging to the network), multiply by 2.5 from 1996 to 2001, while high magnetic signals ($B/\mu > 400$ G, corresponding to strong faculae) increase by a factor of 70. This is a direct consequence of the growing number of ARs present over the solar disk when reaching the maximum.

When comparing contrast plots from different periods of the solar cycle, we realize that the contrast of bright features itself does not seem to change with time. Since the nature of the contrast CLV is related to the structure of the flux tubes making up the magnetic elements, we may infer that the facular flux tube physical properties do not vary with time. As far as we know, this is the first study of the evolution of the contrast of faculae and the network, both on its μ and B/μ dependences, with the solar cycle.

To better fix this assertion, we have superposed the annual quadratic fits to each B/μ interval performed in the $C_{\mathrm{fac}}(\mu)$ plots (see figures 5.4, 5.5 and Appendix C). Figure 5.6 shows the result of this superposition; the color code is indicative of the different years. As can be seen, the different curves for a given B/μ interval are not arranged in any specific temporal order, therefore, there is not any temporal trend for the contrast CLV. This is even more evident in figures 5.7 and 5.8; these figures, respectively, represent the μ-values at which curves of figure 5.6 peak, $\mu_{\max}$, and the maximum contrast values, $C_{\max}$, as a function of time. Note that some points in figures 5.7 and 5.8 have not been plotted, since in some cases the corresponding fits are closer to a straight line than to a quadratic one, obtaining $\mu_{\max}$ values which obviously do not make any physical sense. In other few cases, the fit yielded to a minimum value, instead. From these figures we conclude that there is no trend in the maximum contrasts or their positions.

Summing up, we conclude that the contrast of small magnetic elements does not change with time and, consequently, the flux tube physical properties for a given interval of magnetic signals do not vary with time.
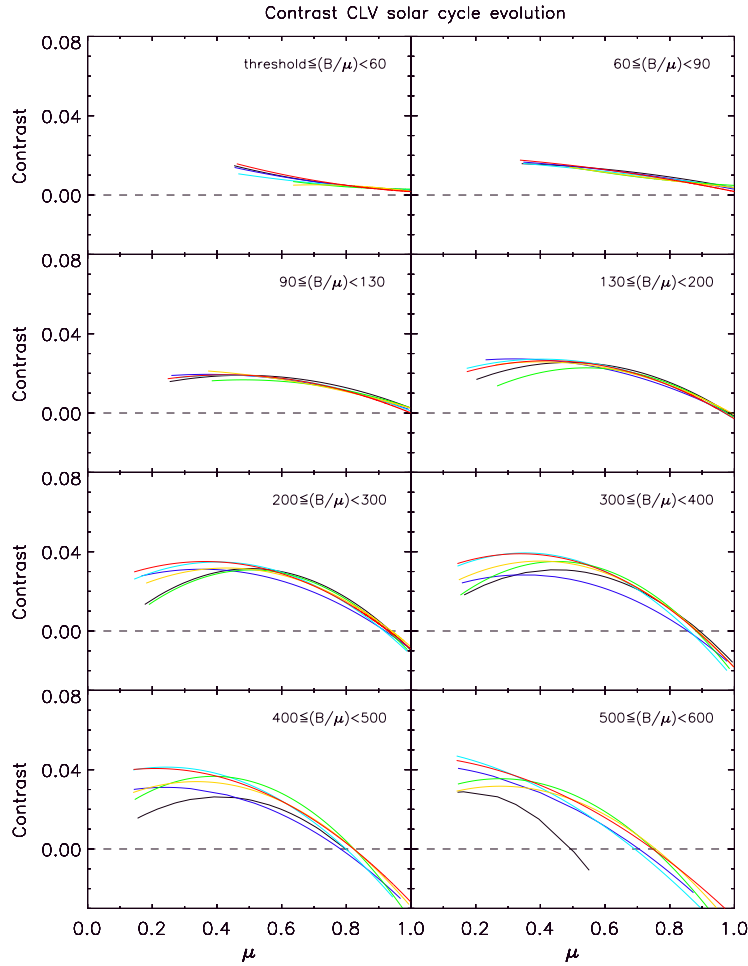
Figure 5.6: Superposition of the annual quadratic fits to every B/μ-bin. They have been taken from the $C_{\text{fac}}(\mu)$ plots; black curves stand for the 1996 fit, dark blue for the 1997 fit, light blue for 1998, green for 1999, yellow for 2000 and red for 2001. No contrast CLV tendency with time may be inferred from these sets.

5.3.1.1 Checking the results

In order to validate the results obtained in Section 5.3.1, we have performed two tests. In the first test we have checked the goodness of the method of rotating and averaging five consecutive 1-minute intensity images. We repeated the $C_{\text{fac}}(\mu)$ and $C_{\text{fac}}(B/\mu)$ analysis using single 1-minute intensities instead of our 5-minute averages, in order to examine if there are any differences with the plots obtained by using 5-minute intensities. There is a perfect agreement, within 5%, between plots derived with both intensity integration times, that mean that the rotation and averaging of consecutive images has been correctly performed.

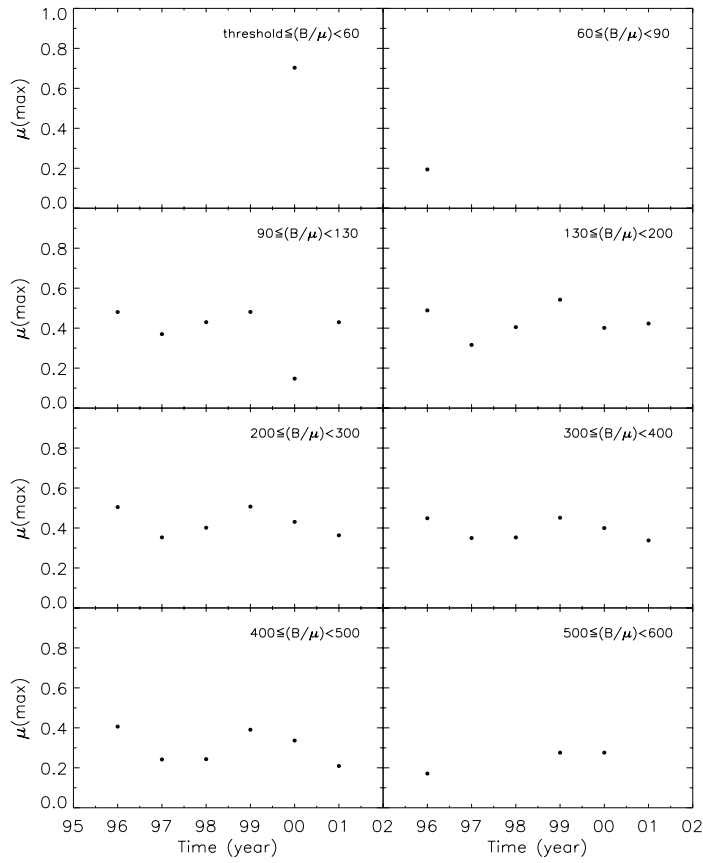The second test is intended to explain the observed differences between figures in

Figure 5.7: μ values that make the contrast maximum are plotted as a function of time. No temporal trends can be deduced.
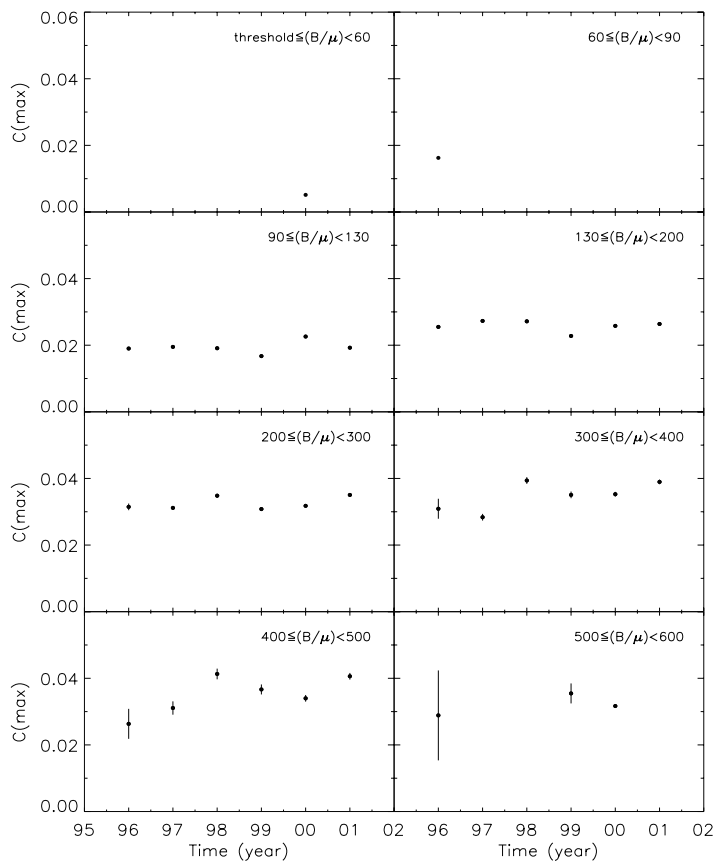

Figure 5.8: Maximum contrasts for each magnetic interval, plotted as a function of time. No temporal trends can be inferred.

Appendix C and figures 4.3 and 4.4. By comparing the aforementioned figures, it can be seen that the contrasts derived in this chapter are systematically lower than those in Chapter 4. In addition, network fields ($B/\mu \leq 90$ G) seem to present a different contrast CLV behaviour. The σ_{mag} maps are used to select magnetically active pixels, thus, their profiles will determine the pixel selection when looking at magnetic signals lying just above the signal-to-noise ratio. The key point is that different profiles will detect different low signal pixels, and we have carried out different determinations of the $\sigma_{\mathrm{mag}}(x, y)$ maps in both analysis (compare Sections 4.2.2 and 5.2.2). According to this, we have now a number of points that have been selected by the present σ^i_{mag} standard deviations (and thus contribute to the network contrast), but not by those used in Chapter 4. In this situation, we can wonder about how those pixels — now selected but not in the former analysis — do contribute to the contrast CLV. In other words, we have to ask the question whether or not those points could explain the differences between low signal contrasts in figure 4.3 and those in figure 5.5, for example.

To give a solid answer to this question, we have chosen those pixels of year 1999 with a magnetogram signal lying between $3\sigma^{1999}_{\mathrm{mag}}$ and the $3\sigma_{\mathrm{mag}}$ threshold derived in Chapter 4. Next step has been determining their contrast in two different ways, according to equation (2.3). While the quiet Sun background intensities, $\langle I_{\mathrm{qs}}\rangle$, are calculated on a daily basis in the present work, it was kept fixed for all 1999 days in the analysis carried in Chapter 4. As expected, the derived contrasts differ slightly. Figure 5.9a represents the contrast for data points using the present daily $\langle I_{\mathrm{qs}}\rangle$ maps, and figure 5.9b represents the same calculation using Chapter 4's fixed $\langle I_{\mathrm{qs}}\rangle$ map. Only the two lowest magnetic signal bins have been plotted, because only low signals just above the thresholds are affected; while figure 5.9a shows a CLV very similar to that presented in figure 5.5, in the μ range where comparisons are possible, figure 5.9b is more similar to the CLV shown in figure 4.3. Keeping in mind that the only difference between both calculations are the non-active intensity backgrounds introduced in equation (2.3), we conclude that a good and accurate determination of QS intensity backgrounds is essential, and, that in this case they are responsible for the differences observed in the contrast CLV of both figures, for network signals. As the intensity background derived in Chapter 4 is, in general, lower than that derived in the present analysis, this explains the systematically higher contrasts reported in that Chapter.
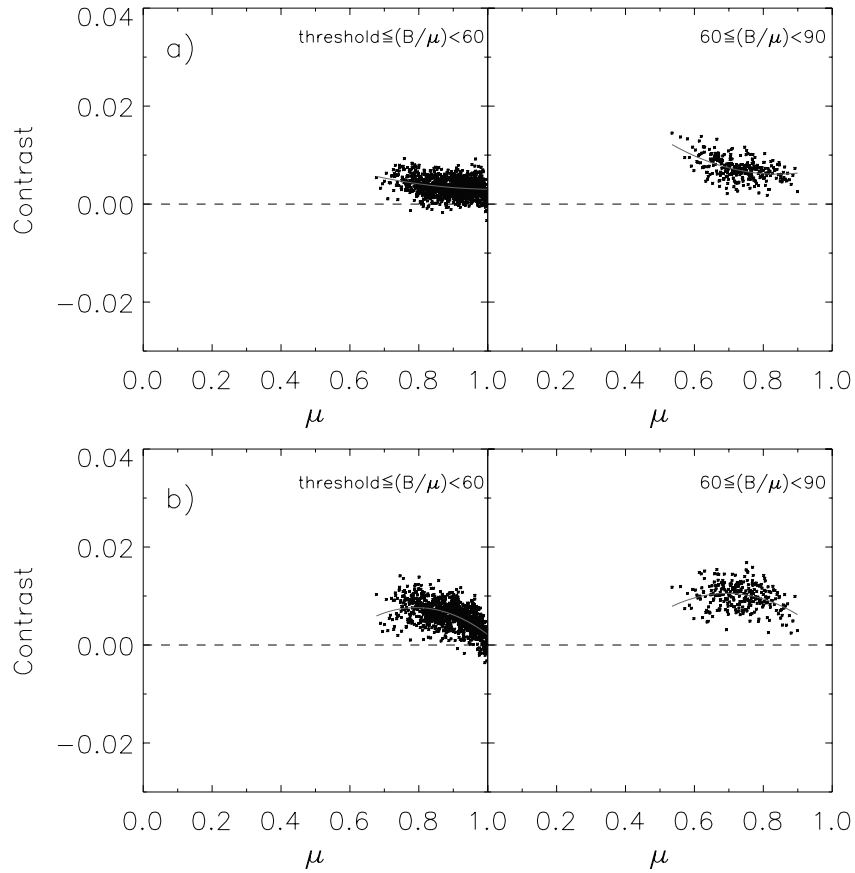
Figure 5.9: Contrast of pixels with magnetogram signals $3\sigma_{\mathrm{mag}}^{1999} \leq (B/\mu) \leq 3\sigma_{\mathrm{mag}}$. **a)** introducing the present daily $\langle I_{\mathrm{qs}}\rangle$ maps into equation (2.3); **b)** with the quiet Sun background surface from Section 4.2.2. Quadratic fits have been overplotted.

5.3.2 Magnetic field distributions

This Section addresses the changes with the solar cycle of the magnetic field that emerges into the phothosphere. As mentioned in Section 5.1, the long-term contribution of the small scale features is poorly known. Several questions arise about them, for example: when, in what form and how they emerge into the photosphere? The matter has been addressed by many authors (e.g., Zwaan 1987; Hoeksema 1994; Harvey & White 1999; Hagenaar et al. 2003) and we contribute to it. We have derived the distribution functions of the magnetic field strength, N(B/μ), where N is the number of pixels, as a function of time. Then, we have quantified the network, faculae and micropore populations object of our study from 1996 to 2001 and we suggest an answer to part of those questions.

We derived histograms of the number of pixels, N, as a function of the magnetic

Table 5.2: Power-law index α of the magnetic field distributions

Time (year)	α ($B/\mu < 250$ G)	α ($B/\mu \geq 250$ G)
1996	2.5	2.8
1997	2.4	2.8
1998	2.3	2.9
1999	2.2	2.9
2000	2.1	2.8
2001	2.1	2.8

signal, B/μ, for each selected magnetogram. The averaged histograms, corresponding to the ten annual magnetograms, yielded one distribution function N(B/μ) for each year, so we obtain these distributions at different phases of the solar cycle. Next step was producing log(B/μ)-log[N(B/μ)] linear fits for each histogram, for field values of B/$\mu \geq 20$ G. This leads to a power-law dependence of the form N(B/μ) $\propto (B/\mu)^{-\alpha}$. These distributions show a knee at around 250 G, therefore, the linear fits deviate from the data; this behaviour becomes much clear as we move towards the solar maximum. To overcome this deviation, we proceeded to divide the magnetic field interval in two ranges, below and above 250 G, in order to obtain better fits to these histograms. For $B/\mu < 250$ G, the power-laws derived in this way show an index α which varies between 2.5 and 2.1 from the solar minimum to the maximum (see table 5.2), decreasing with the increasing phase of the solar cycle. For the $B/\mu \geq 250$ G, this solar cycle dependence is weak, if exists.

Figure 5.10 illustrates the above-mentioned distributions of the magnetic field strength at different times in the solar cycle; this is a log-linear plot showing the histograms for each year. The two fitted power-law dependences (below and above 250 G) are overplotted. Note that the highest magnetic signal for each distribution increases with solar activity, due to the increasing number of faculae. At the same time, the relative fraction of low signal pixels keeps constant or even decreases (see Section 5.3.3). We also tried to fit exponential dependences, N(B/μ) $\propto$ e$^{(-B/\mu)}$, for the distribution functions N(B/μ) in order to compare our results with those of other authors who used such functional dependences (Hagenaar 2001; Hagenaar et al. 2003). In our case exponential fits produce much worse results than the power-
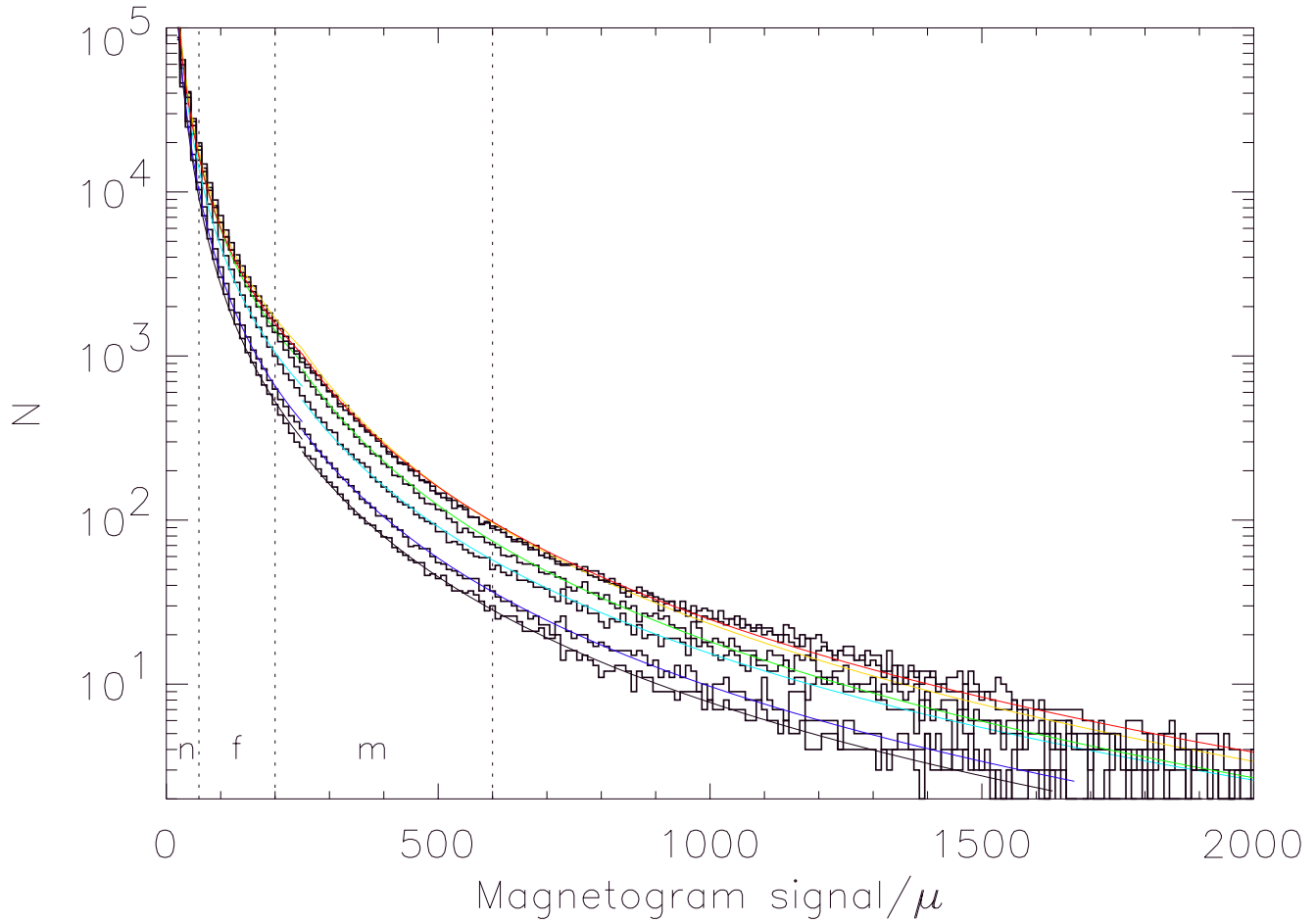
Figure 5.10: Average histograms of $N(B/\mu)$ versus the magnetic signal B/μ, for each year between 1996 and 2001 (bin width is set to 10 G for clarity). The power-law fits are overplotted. The index α changes at 250 G (table 5.2). Color code is as in figure 5.6; n, f and m stand for the network, faculae and micropore components, respectively.

law fits used, so we discarded them. The most probable reason is that these authors limited their study to low magnetic field values, where an exponential is also a good choice.

From the derived fits, we quantified the network, faculae and micropore populations for half a solar cycle by summing all points in the histograms between some given B/μ-limits. The chosen limits were $[20, 60]$ G for the network, $[60, 200]$ G for faculae and $[200, 600]$ G for the micropore population; these limits are somewhat arbitrary. According to Topka et al. (1997) micropores have a negative contrast at disk center but positive near the limb. Our results show that negative contrasts around $\mu = 1$ start at $B/\mu \geq 200$ G (see for example figures 4.4 or 5.5) while fea-
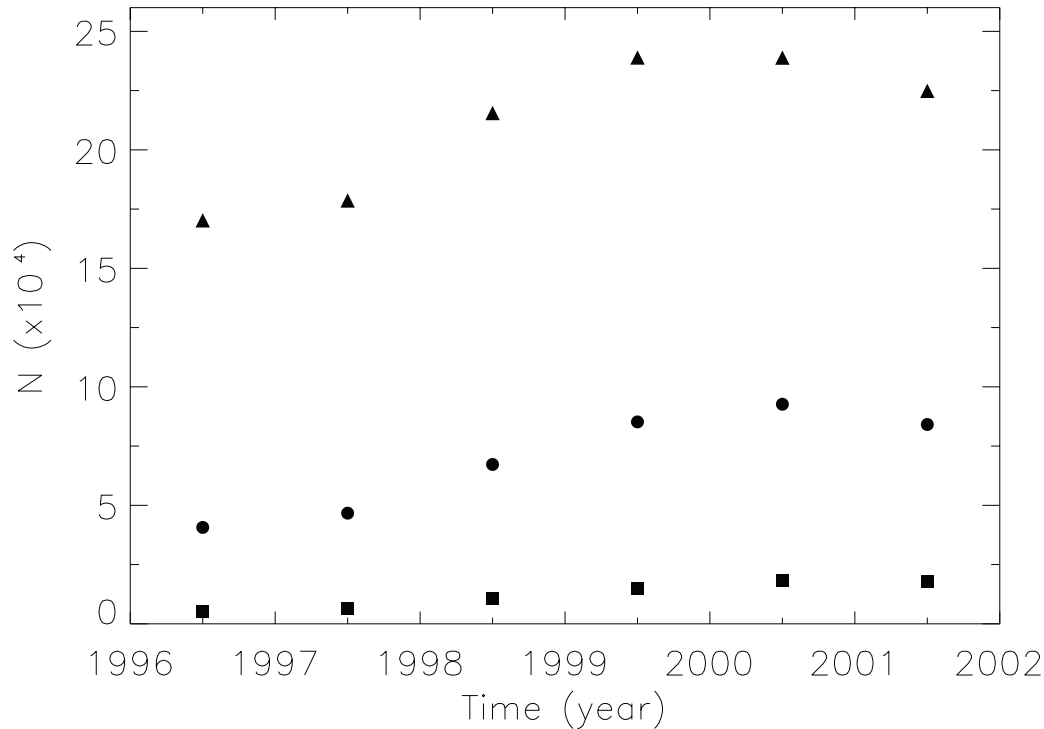
Figure 5.11: Network, faculae and micropore populations during the rising phase of cycle 23. Filled triangles, circles and squares represent network elements, bright faculae and micropores, respectively.

tures below 200 G still present a positive contrast at disk center. This is the reason for choosing 200 G as the limit between bright faculae and micropores. 600 G is our upper limit for the study of photospheric bright features. Letters n, f and m in figure 5.10 stand for the network, faculae and micropore populations. Figure 5.11 illustrates the number of points considered as network elements, bright faculae and micropores as a function of time. As expected, the number of all types of features increases with solar cycle. The dominating population is the network, because its number is three times higher that the number of faculae, at all times; moreover, they are always present over the disk, while micropores only appear in the rising phase of the cycle. We will come back to this point in Section 5.3.3, when discussing the role of the network and faculae in the long-term solar irradiance variations.

5.3.3 Solar surface structures: image decomposition

In order to specify the contributions to irradiance variability by specific types of (small) solar surface magnetic structures, we have decomposed our sixty magnetograms in two components, namely, active regions and quiet Sun network. This decomposition is based on the magnetic field strength of the components and its distribution over the disk. In parts of this Section we have combined the results of applying the mask that identifies the surface distribution of bright magnetic features (Section 4.2) with the results of this decomposition. It is our aim to quantify the proportions of the small scale magnetic elements − the network and faculae − along the solar cycle, in order to compare their role in the long-term irradiance variations, because variations in the proportions of the various structures on the Sun produce variability in its radiative output. Using the magnetogram decomposition, we have also examined the evolution of the contrast for both components, active regions and quiet Sun network.

The method to separate active regions from quiet Sun components is based on the work of Harvey (1994); specifically we used a routine provided by N. Krivova (private communication), adapted to our purposes. There are other methods to classify and separate activity structures over the solar surface, which consider from simple thresholds (Johannesson et al. 1995), statistical pattern recognition techniques (Turmon et al. 2002), to identification based on flux strength, contiguity, filling factor and association with sunspots (Harvey & White 1999), and contrast and contiguity criteria (Preminger et al. 2001). According to the employed technique, active regions are identified in the magnetograms by evaluating the amplitude of the variations of the magnetic signal within subarrays of 40×40 pixels. This takes advantage of the fact that inside an active region, the magnetic field is not uniform because it presents great fluctuations.

Following Harvey's work we proceeded in three steps: [1] We computed the root-mean-square-differences in the mentioned running boxes of 40×40 pixels, and assign the results to the central pixels in each subarray; the result is a map of the root-mean-square-differences determined for every pixel in the magnetogram. [2] This map is then smoothed using a 20 pixels width smoothing window in order to remove irregularities. [3] The smoothed map is thresholded to define the location of active regions. We tried three different levels (1000, 1500 and 2000 in r.m.s. units) to choose the best threshold; figure 5.12 shows the result of applying this method to a
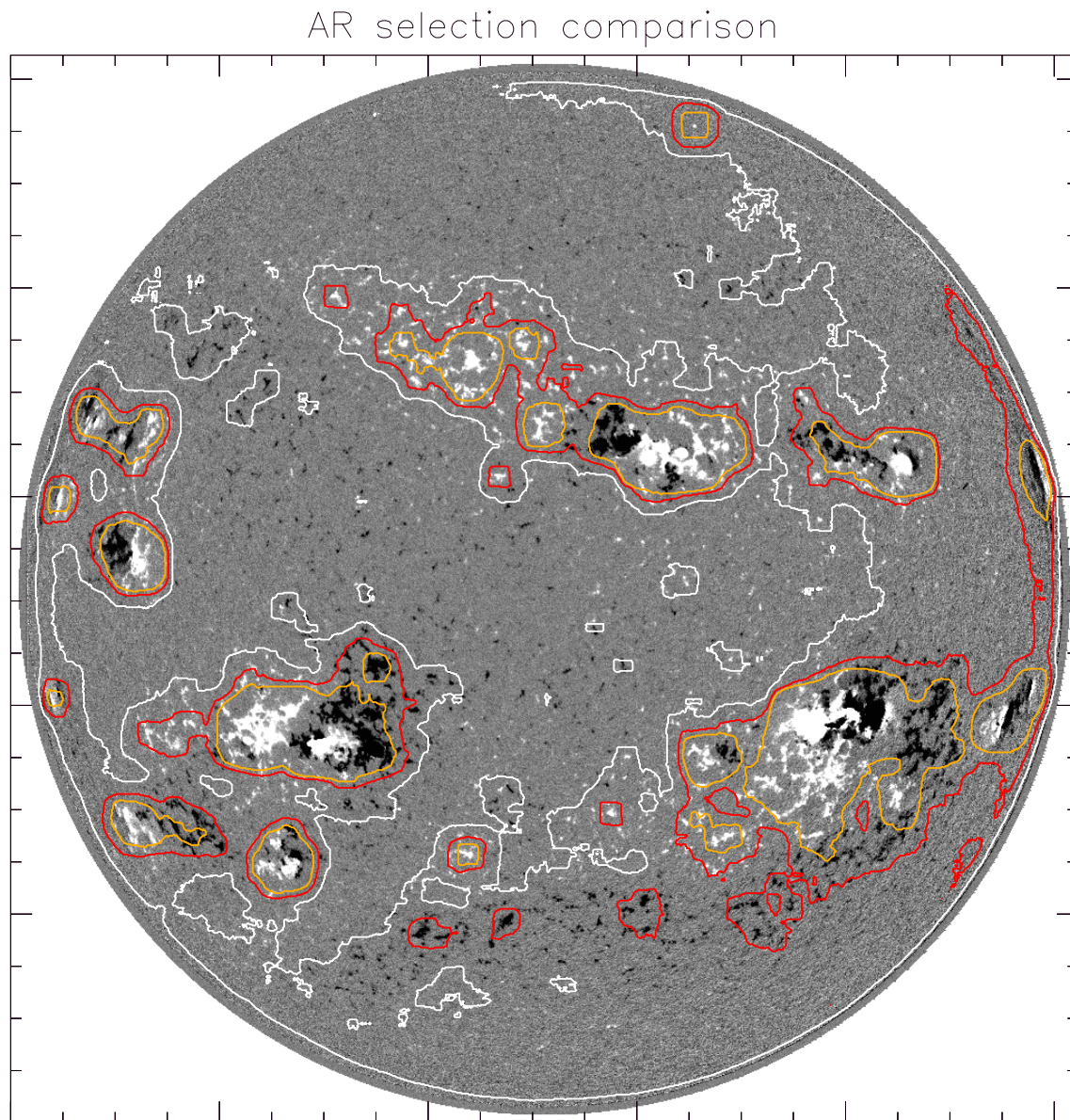
Figure 5.12: Example of application of the magnetogram decomposition method for the separation of active regions. Three thresholds are tried to define the location of AR's: 1000, 1500 and 2000 r.m.s. levels are represented by white, red and orange boundaries, respectively.

magnetogram. The threshold which best identifies the boundaries of the observed active regions seems to be 1500, since lower values include parts of the solar surface clearly not belonging to any magnetic concentration, and higher thresholds are too strict, producing fragmented regions which should be compact. Quoting Harvey (1994): "compared to just thresholding the data at a given field value, this method to isolate active regions results in less patchy selection of pixels considered to be in an active region, as well as an active region boundary that is expanded slightly outside the isogauss contour". The decomposition of the magnetograms in two components allows us to separately analyze the contrast evolution for each type of structure as a function of position and magnetic signal. The procedure followed is the same as for the contrasts obtained in Sections 4.3 and 5.3.1.

We divided the period of six years in three parts: "Minimum" (1996 and 1997), "Mid" (1998 and 1999) and "Maximum" (2000 and 2001); for each subperiod we chose four days (especified in table 5.3). We superposed the mask that identifies small bright magnetic features (see Chapter 4) with the result of the image decomposition, for each day. Proceeding this way for each subperiod, pixel distributions share out either in network or facular features, belonging to the active region component, or in network or facular features that belong to the quiet network component. Finally, data coming from each group of four days are put together. Therefore, small magnetic features are classified by their magnetic signal and intensity, as well as by their location over the solar surface.

Figures 5.13 and 5.14 show two examples of the CLV contrast of different magnetic features for the quiet Sun component during the solar minimum, and for the active region component during the solar maximum, respectively. The complete $C_{\text{fac}}(\mu)$ and $C_{\text{fac}}(B/\mu)$ series can be found in Appendix D. They are separated in the active region component and the quiet Sun component (indicated as AR or QS, respectively) for the three mentioned subperiods (Minimum, Mid or Maximum); the number in the top left corner of each box represents the number of pixels in this B/μ interval.

The contrasts of the AR or QS components behave, as a function of either μ or B/μ, as the evolution of the contrast described in Section 5.3.1; this can be easily seen by comparing the figures in Appendix D with those in Appendix C. In fact, there are no relevant differences in the derived contrast CLV, but in the amount of data points contained in each interval. The AR component presents the greatest
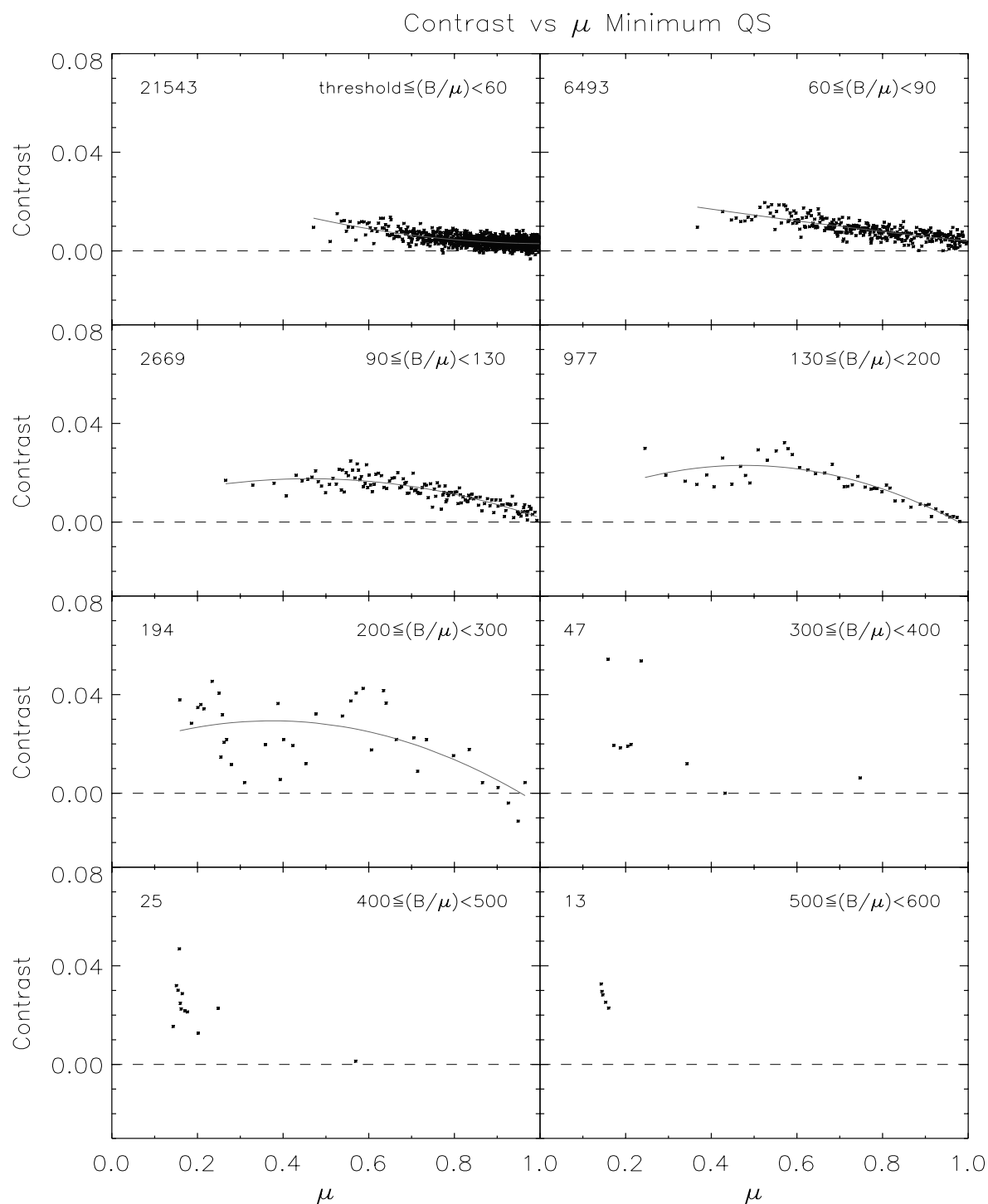
Figure 5.13: Facular contrast around solar minimum as a function of μ, for the QS component. Magnetic signals have been divided in eight intervals. A dashed line indicates $C_{\mathrm{fac}} = 0$. Solid curves represent a quadratic fit to the points; $\mu = 1$ is the disk center, $\mu = 0$ is the limb. The number in the upper left corner counts the number of pixels in each B/μ interval.
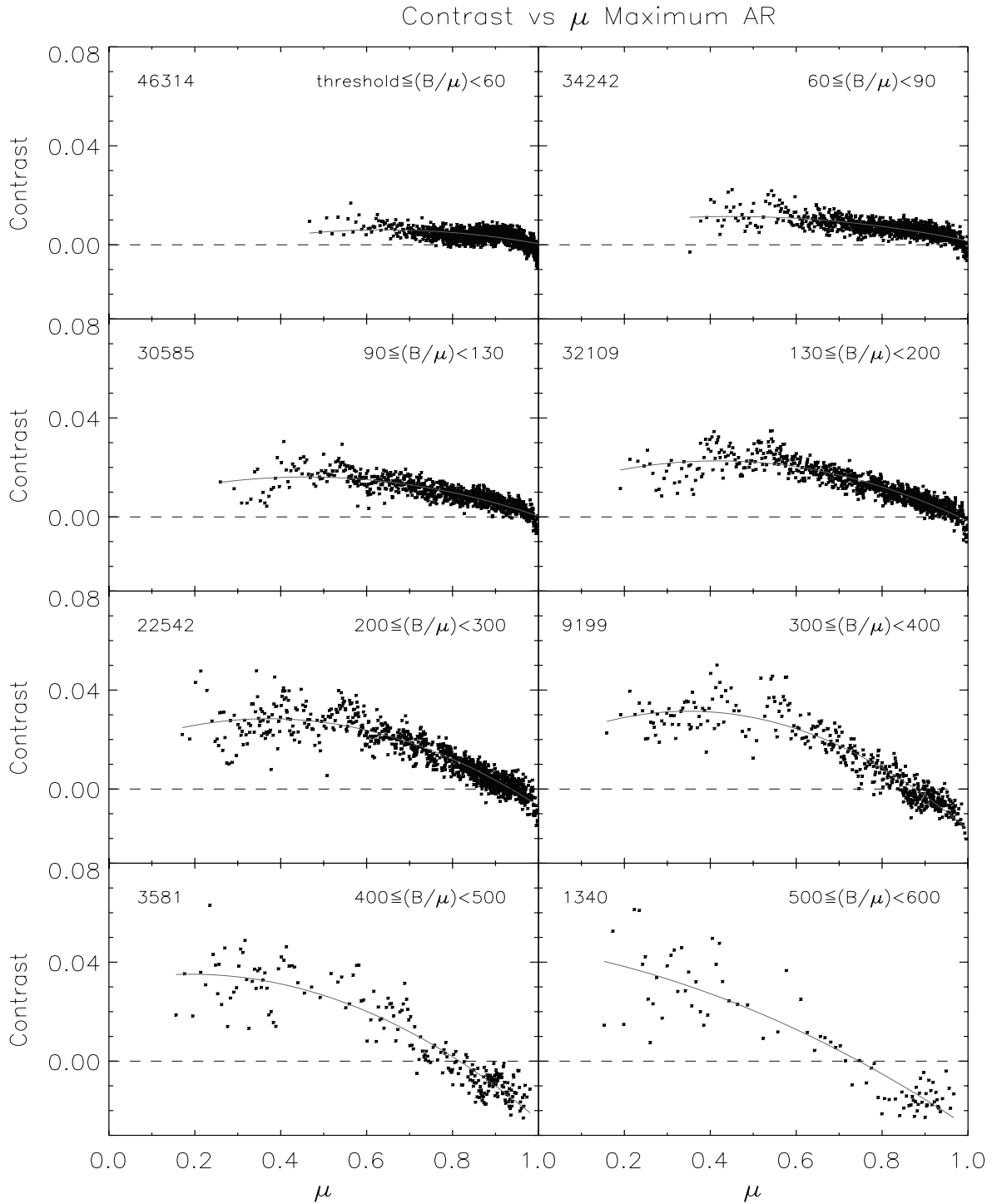
Figure 5.14: The same as figure 5.14 for the AR component around solar maximum.

Table 5.3: Selected data for each subperiod within the rising phase of cycle 23

Subperiods	Selected data
Minimum (1996 & 1997)	06/08/1996
	21/10/1996
	22/04/1997
	14/09/1997
Mid (1998 & 1999)	18/05/1998
	03/11/1998
	12/04/1999
	20/11/1999
Maximum (2000 & 2001)	17/05/2000
	30/11/2000
	25/09/2001
	09/11/2001

changes in the quantity of points involved from minimum to maximum. This is a straightforward consequence of the fact that the number of active regions increases towards solar maximum. Points of the QS component tend to accumulate at low field values, while points of the AR component tend to accumulate towards high magnetic signal values. For example, for $B/\mu < 60$ G, the QS plot contains 67% of the points, while only 33% are contained in the AR plot. The opposite is true, 0.1% and 4% for the QS and AR components respectively, for $B/\mu > 400$ G. This bias is intrinsic to the separation in both components, since they differ in the magnetic signal of the flux tubes underlying these populations.

As in Section 5.3.1, we find that the contrast is time independent, and even component independent, since both QS and AR structures show similar contrast CLV. We reafirm the conclusion given in Section 5.3.1, that the physics of the flux tubes that underly these populations does not change with time. Moreover, a flux tube shows the same CLV whether it is located in the active region or in the quiet Sun component. What changes from one structure to the other is basically the degree of compactness, the range of sizes of its elements and the magnetic flux they contain. Our active region component contains pixels with both high an low magnetic signals, in agreement with the typical fluctuations of field strength inside

active regions. The QS component presents mainly low signal pixels, but also a few higher ones, most probably because the performed procedure misinterprets the features of a small fraction of the smallest magnetic concentrations.

For each structure class, AR and QS network, we repeated the histogram analysis described in Section 5.3.2. The aim is to show how the distributions of magnetic signal in both components evolve with time. The corresponding histograms of magnetic signal (without mask superposition) for the two structure classes and three subperiods are shown in figure 5.15. In this case "Minimum", "Middle" and "Maximum" correpond, respectively, to 6 August 1996, 20 November 1999 and 25 September 2001; left and right columns show the distributions for the QS and AR components, respectively. Note the widening of the wings in the distributions for active structures towards the maximum. These results are similar to the results found by Harvey & White (1999) (see their figures 9 and 10); the differences are that we take into account three subperiods between solar minimum and maximum instead of two, while they decompose the solar surface in four structure classes instead of two.

Finally, we used the magnetogram decomposition to quantify the evolution of the network and the facular populations. It has been theoretically assumed and it is expected that these populations − especially the network − substantially contribute to increase the observed irradiance during solar maximum activity. The procedure used is as follows: first, we have superposed the mask that identifies small bright magnetic features (see Chapter 4) with the result of the image decomposition for each of the sixty selected days. We obtain either network or facular points belonging to active regions, or network or facular points belonging to the quiet network component. Then we proceed to define the network and the facular populations; we defined as "network" all selected pixels that were in the QS component, as well as those in the AR component with $B/\mu < 90$ G. In this way we take into account both the enhanced and the quiet network. Those pixels inside the AR component with $B/\mu \geq 90$ G have been defined as "faculae". Therefore we obtain three values for each day, namely, the total number of small bright magnetic features, the number of pixels identified as network, and the number of pixels identified as faculae; we present these results in figures 5.16 and 5.17. Figure 5.16 shows the fraction of network and facular pixels relative to the total number of identified small features for each day, and figure 5.17 shows the absolute number of pixels of both types for each day. The fraction of faculae is correlated with the solar cycle; however,
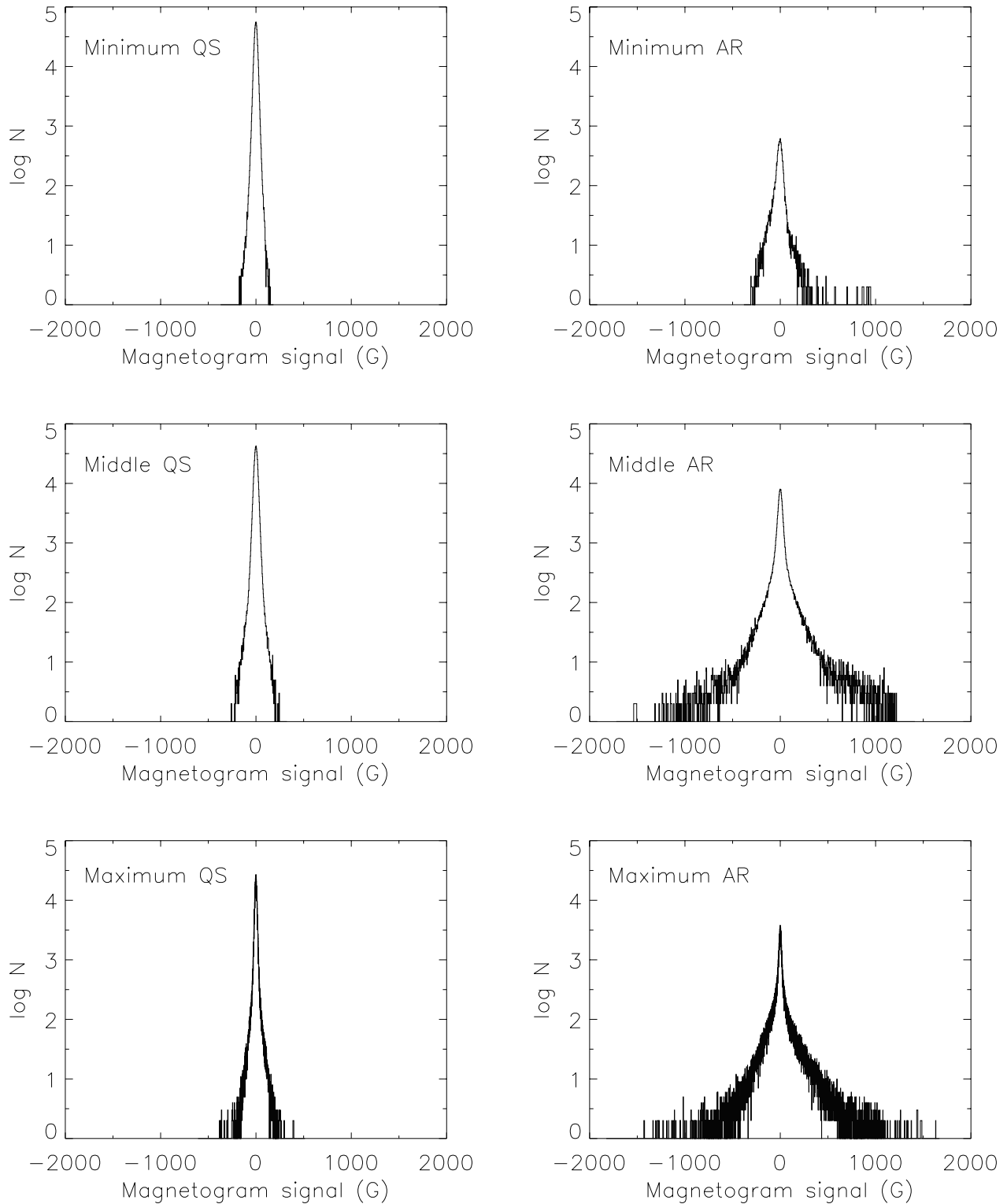
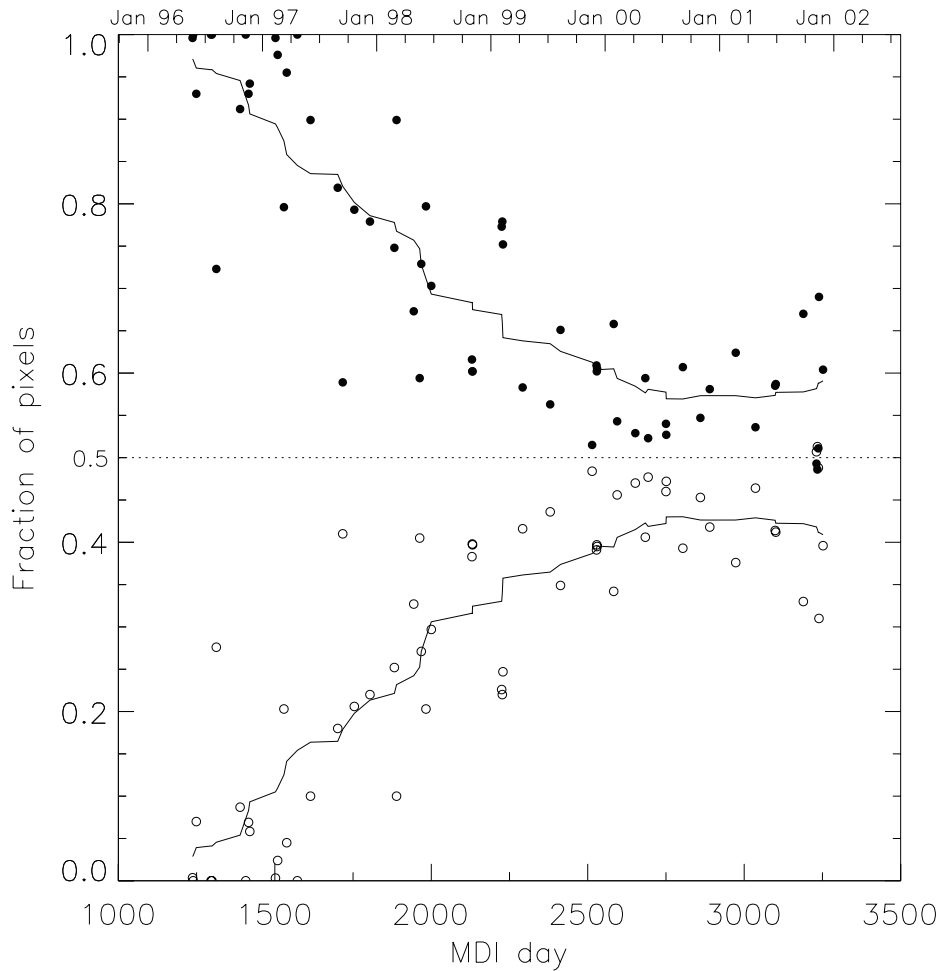Figure 5.15: Histograms of magnetic signal of the two components, as a function of time.

Figure 5.16: Fraction of network (filled circles) and faculae (empty circles) relative to the total number of identified small bright features for the sixty days analyzed. The solid curve represents a running mean. The dotted line is the 50% mark.

the fraction of network features is in anticorrelation with the cycle. For example, around the minimum, 90% (even more) of the detected bright features belong to the network, and only a 10% (or less) are detected as faculae; near the maximum the proportions tend to equilibrate, about 55% are network pixels while 45% are faculae. This is in agreement with the fact that at solar minimum only a few active regions are seen over the solar disk, and most of the area is occupied by the quiet Sun network component. As solar activity increases, active regions occupy a larger fraction of the solar surface, to the detriment of the area occupied by the quiet Sun component. When considering the absolute number of pixels, we see that the amount of facular pixels increases from almost zero at minimum to about $2\,10^4$ around solar maximum, while network pixels increase from about $1\,10^4$ to less than $3\,10^4$ at maximum, showing therefore a slower growing rate. Thus, we conclude that
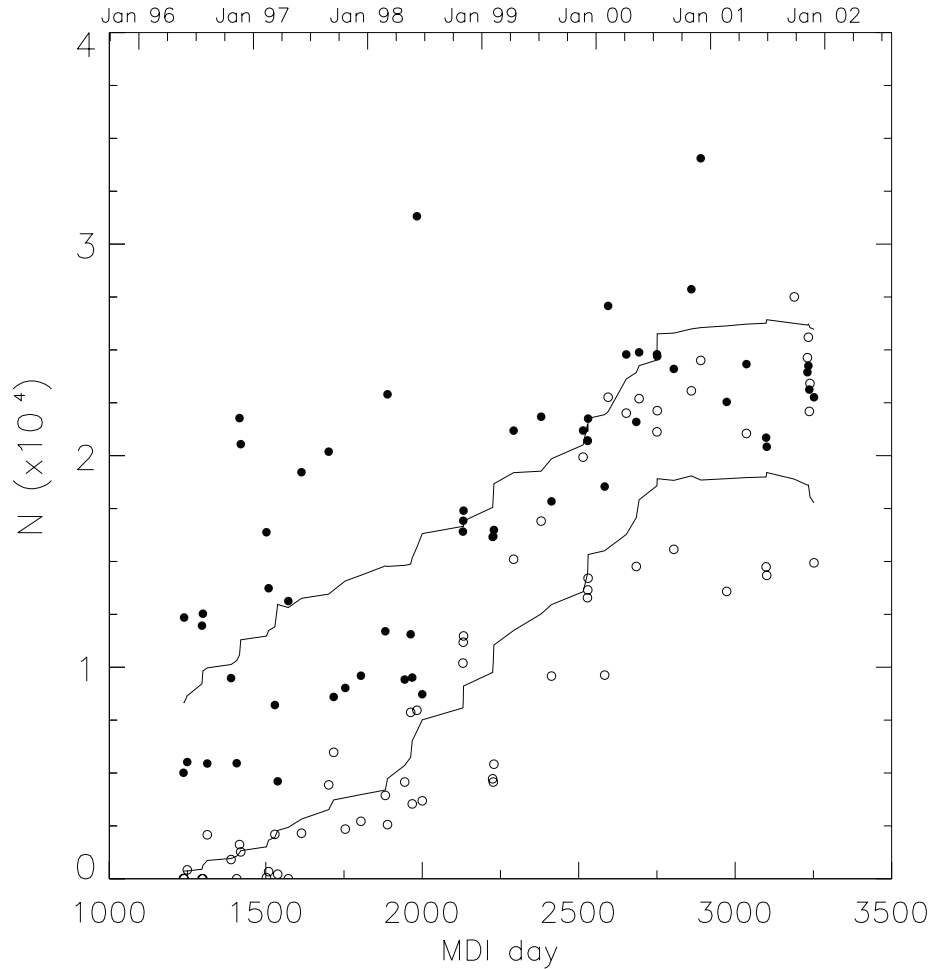
Figure 5.17: Absolute number of network pixels (filled circles) and faculae (empty circles) for the sixty days analyzed. The solid curve represents a running mean.

the network is always present over the solar disk, and always in a higher quantity than faculae, becoming the dominant component through the solar cycle. This is true even at the activity maximum period, and in spite of having a lower increase rate relative to that of faculae.

5.4   Discussion and Conclusions

We found that the distributions of the magnetic signal, $N(B/\mu)$, have a functional power-law dependence on B/μ, and that the power-law index decreases with increasing solar activity. Schrijver & Harvey (1989), using low resolution synoptic magnetic field maps from Kitt Peak for the period between 1975 and 1984, found that the

distribution of the magnetic field strength follows a power-law, and stated that the power-law index decreases as the mean absolute magnetic flux increases. Murray (1992), proceeding in a similar way, confirmed this assertion. Our results go in the same direction, because the total magnetic flux is coupled with the solar activity cycle, as it increases when approaching the solar maximum (see, for example, figure 3 in Harvey 1994).

The image decomposition method performed gives results useful enough for our purposes. Harvey & White (1999) carried out a probably more elaborated analysis by decomposing the solar surface in four components, in order to specify quantitatively the contributions to irradiance variability by specific types of solar surface structure. Their data sets were full-disk magnetograms and Ca II K images from the National Solar Observatory and Big Bear Solar Observatory for several days in early 1992 and mid-1993. A close inspection of their figure 17 shows that our AR component agrees most probably with their active region and decaying active region components; our quiet Sun network component mostly coincides with their network plus part of the enhanced network components. Meunier (2003), using MDI full-disk magnetograms taken between 1996 and 2002, studied the evolution of the properties of magnetic field structures along the solar cycle, and found that the magnetic flux of small structures increases from solar minimum to solar maximum (in this work, structures must include four or more contiguous pixels above a certain level). This study also found a power-law dependence for the sizes and for the magnetic fluxes of all types of structures, which are fully compatible with our findings.

Walton et al. (2003) have recently analyzed Ca II K images at 393.4 nm using a 1 nm bandpass in order to study changes in the facular and network sizes during the decline of cycle 22. They defined the network and the faculae according to their size and latitudinal distribution, and found that large-scale bright features − faculae − dominate the change in the total solar irradiance between solar minimum and maximum, producing about 80% of the total change. These results are not so different from ours, because their study is exclusively photometric and their selection criteria is based on the size of the structure, while our selection criteria relies on the magnetogram signal and location of the features. Therefore the comparison is difficult because these two selection criteria are completely different. It is worth noting that exclusively photometric studies suffer from a bias towards brighter features.

In Sections 5.3.1 and 5.3.3 we have seen that, as far as irradiance is concerned,

small magnetic features − network bright points and faculae − are invariant respect to the evolving solar cycle, and even that their radiative properties are independent of whether they are located (within active regions or in the quiet Sun region). This is a relevant result because there is no theoretical argument that implies that small magnetic features should have a different structure at solar minimum and at maximum, or at different locations. It is not excluded that the photospheric magnetic field behaves differently due to its possible distinct origin; for example, it can be conceived that the magnetic field emerging in active regions is the result of the emergence of the field rooted at the bottom of the convection zone, and thus all field present in the photosphere is the result of active region dispersion. Alternatively, small magnetic elements in the quiet Sun areas could be the result of small local dynamos powered by convection.

In Sections 5.3.2 and 5.3.3 we have computed the change in the number of magnetic single elements that produce the network, faculae and micropores. Each of these features was defined by their magnetic field per pixel. It is important to notice that we study single elements framed in $2 \times 2''$ pixels. The populations of the three types of elements increase with the solar activity. The combination of the CLV contrast results and the evolution of the feature populations is an evidence of their contribution to the total solar irradiance variations. The increase rate of the network population is slower than that for faculae and micropores, but since network elements are much more abundant, they must have a significant contribution to the total irradiance, an are good candidates to be the main responsible for the increase in the solar irradiance from minimum to maximum.

Finally we conclude that, due to the slight but significant differences between the CLV variations found at low magnetic fields in Chapter 5 and those found in Chapter 4, a careful analysis of the response of the detector with time is imperative in any study of the long-term contributions of faculae and the network to irradiance variations. Of special importance is an accurate determination of quiet Sun intensity backgrounds, which we believe is essential.